



CHORUS

This is the accepted manuscript made available via CHORUS. The article has been published as:

Enhanced ferroelectric polarization in epitaxial $(\text{Pb}_{1-x}\text{La}_x)(\text{Zr}_{0.52}\text{Ti}_{0.48})\text{O}_3$ thin films due to low La doping

Devajyoti Mukherjee, Mahesh Hordagoda, David Pesquera, Dipankar Ghosh, Jacob L. Jones, Pritish Mukherjee, and Sarath Witanachchi

Phys. Rev. B **95**, 174304 — Published 23 May 2017

DOI: [10.1103/PhysRevB.95.174304](https://doi.org/10.1103/PhysRevB.95.174304)

Enhanced ferroelectric polarization in epitaxial $(\text{Pb}_{1-x}\text{La}_x)(\text{Zr}_{0.52}\text{Ti}_{0.48})\text{O}_3$ thin films due to low La doping

Devajyoti Mukherjee^{1,2,*}, Mahesh Hordagoda³, David Pesquera², Dipankar Ghosh⁴, Jacob L. Jones⁵, Pritish Mukherjee³, and Sarath Witanachchi³

¹*Technical Research Center, Indian Association for the Cultivation of Science, 2A & 2B Raja S. C. Mullick Road, Kolkata 700032, India*

²*Department of Materials Science & Metallurgy, University of Cambridge, 27 Charles Babbage Road, Cambridge CB3 0FS, UK*

³*Center for Integrated Functional Materials & Department of Physics, University of South Florida, Tampa, FL 33620, USA*

⁴*Department of Mechanical & Aerospace Engineering, Old Dominion University, Norfolk, VA 23529, USA*

⁵*Department of Materials Science and Engineering, North Carolina State University, Raleigh, NC, 27695, USA*

* Author for Correspondence: trcdm@iacs.res.in

ABSTRACT

Enhanced polarization is reported in ferroelectric $(\text{Pb}_{1-x}\text{La}_x)(\text{Zr}_{0.52}\text{Ti}_{0.48})\text{O}_3$ (PLZT) thin films at low La doping concentrations. Epitaxial PLZT thin films with varying La concentrations were grown in both (001) and (111) crystallographic orientations using the conducting perovskite oxide $\text{La}_{0.7}\text{Sr}_{0.3}\text{MnO}_3$ as the top and bottom electrodes on SrTiO_3 substrates by pulsed laser deposition. Dilute doping of La (0.1 – 0.5 at. %) was found to enhance the remanent polarizations in the PLZT films irrespective of their orientations. An increase in the remanent polarization by a factor of 2 is observed in the 0.5 at. % La doped PLZT thin film as compared to the undoped PZT film. The increase in polarization in the PLZT thin films was associated with the tetragonal distortion of the PLZT lattice due to the substitutional doping of La at the Pb sites, as evidenced from x-ray and microstructural analyses. Using the structural and polarization data, a linear correlation between the square of the remanent polarization and crystal-lattice distortion is obtained in the PLZT system which corroborates with the Landau-Ginsburg-Devonshire thermodynamic model of lattice distortion-induced change in spontaneous polarization. The work provides a novel route to enhance polarization in PLZT films which is crucial for the coherent design of high-performance PZT-based ferroelectric and piezoelectric devices.

Keywords: ferroelectric thin films, epitaxy, remanent polarization, lattice distortion, structure-property relationships, strain

I. INTRODUCTION

$\text{Pb}(\text{Zr}_{0.52}\text{Ti}_{0.48})\text{O}_3$ (PZT) is the state-of-the-art material for applications in high-power transducers, micro-electro-mechanical devices, and non-volatile memories; owing to its high ferroelectric (FE) polarization and piezoelectric coefficients [1-5]. Regardless of the recent environmental concerns on the toxicity of lead, PZT has remained the industry-standard piezo- and FE ceramic; since few of the currently available Pb-free FE materials have shown properties comparable to PZT [5,6]. PZT has high mechanical and chemical stability allowing its safe encapsulation for device fabrication and the Pb in PZT is stable in the oxide form. PZT thin films and nanostructures are used in sensors, actuators, field-emitters, high-frequency electrical components, tuneable microwave circuits [8-14] and have also been proposed for use in magneto-electric (ME) memories and in electrocaloric solid-state coolers [15-20]. Realization of novel device applications and improvement of the existing technologies have thus created a constant demand for high quality PZT thin films exhibiting enhanced polarization properties.

In this regard, property modification of PZT for specific applications by doping the "A" (Pb) or "B" (Zr/Ti) sites of the ABO_3 -type PZT unit cell with rare earth elements has been intensely investigated [21-24]. Donor-type dopants such as La^{3+} , Nb^{5+} , Ce^{3+} , Ta^{5+} can enhance the electronic properties of PZT by enhancing domain wall mobility [22-24]. In particular, La-doped PZT (PLZT) has been a widely studied FE ceramic for its high optical transparency and desirable electro-optic properties, making it well-suited for applications in light shutters, coherent modulators, colour filters, and image storage devices [25,26]. Aliovalent doping of La in PZT influences its microstructure to enhance the dielectric and the piezoelectric properties, both in bulk and thin film forms [27-31].

In PLZT ceramics the substitution of La^{3+} for Pb^{2+} ions necessarily lead to vacancies on the A-sites, causing displacement of the ions in the PLZT unit cell and therefore lattice distortion [32]. In general, when a La^{3+} ion replaces a Pb^{2+} ion in the perovskite PZT unit cell, it induces lead vacancies (V_{Pb}'') in order to maintain its electrical neutrality [25,26,30]. The density of such defects is governed by the La doping concentration [30]. The presence of the $\text{La}_{\text{Pb}}^\bullet$ defect in the vicinity of the V_{Pb}'' leads to immobile ($\text{La}_{\text{Pb}}^\bullet - V_{\text{Pb}}''$)-type defect dipoles within the PLZT unit cell. These defect dipoles generate random fields that may destabilize the local domain structure. The lowered stability of the domain structure against external fields then could potentially facilitate the domain wall motion in PLZT, and influence its piezoelectric and FE properties [26-31]. However, the underlying mechanism for this effect is still not completely understood, and is the subject of continuing research [33].

The effects of La doping on the FE properties of PLZT bulk ceramics have been well studied [34-39]. Increased squareness of the FE hysteresis loop and decreased coercive fields have been reported in bulk PLZT ceramics at low La doping [34-37]. Rossetti et al. have reported that substitution of as little as 0.2 at. % La in bulk PZT ceramics can create significant tetragonal distortion of the crystals, and change their spontaneous polarization (P_s) [36]. Although the origins of such spatial variations of the P_s in PLZT ceramics were unclear, Rossetti and co-workers evidenced changes in the micro-domain structure of PZT as a result of low La substitution [38,39].

While the investigation of the microstructure-property relationships in PLZT thin films is necessary for device applications, a detailed literature survey shows the role of La in the FE property modification of PLZT thin films have not been unequivocally established. This is primarily due to the scarcity of high-quality single crystalline PLZT thin films and contradictory

experimental results [40-44]. While some groups have reported on the enhanced polarization in PLZT films with increasing La doping concentrations, [43] others have implied that La doping lowered the remanent polarization, due to the reduction in tetragonality of the PLZT unit cell [44]. Polycrystalline PLZT thin films have been grown using numerous chemical synthesis routes such as sol-gel method, [40,45,46] chemical solution deposition, [28,29,47] and metal-organic chemical vapor deposition [48]. However, proper control of the microstructure, grain size, porosity, and crystallinity have remained major issues [28,29,40,45-48]. Physical deposition techniques such as pulsed laser deposition (PLD) are also challenging for the growth of PZT thin films due to the high volatility of Pb in PZT that leads to its non-stoichiometric ablation and results in Pb-deficient PZT films exhibiting poor FE properties [49,50,51]. Among the few reports on the PLD grown PLZT thin films almost all of them discuss polycrystalline PLZT thin film properties [41,52-54]. Here, we perform an in-depth study on the growth of epitaxial PLZT thin films with systematic control of crystallinity, stoichiometry, grain size, surface roughness, and doping concentrations.

Stoichiometric epitaxial $(\text{Pb}_{1-x}\text{La}_x)(\text{Zr}_{0.52}\text{Ti}_{0.48})\text{O}_3$ thin films with low La-doping concentrations varying as 0.1 atomic (at.) %, 0.5 at. % and 1.0 at. % were grown by PLD. Symmetric PLZT thin film capacitors were fabricated *in-situ* using the half-metallic oxide $\text{La}_{0.7}\text{Sr}_{0.3}\text{MnO}_3$ (LSMO) as the top and bottom electrodes on single-crystal SrTiO_3 (STO) (100) and STO (111) substrates [55]. We report highly enhanced remanent polarization ($P_r \approx 91\mu\text{C}/\text{cm}^2$) in 0.5 at. % PLZT (001) thin film as compared to that in undoped PZT (001) thin film ($P_r \approx 49\mu\text{C}/\text{cm}^2$) measured under similar conditions. To our knowledge, such high polarization values in PLZT thin films have been reported for the first time. A strong correlation between the enhanced remanent polarization and the crystal lattice distortion of the PLZT unit cell at varying

La concentrations is established. The work provides fundamental understanding into the origins of large polarization in PLZT thin films and predicts property design for novel FE devices for potential data-storage, electro-optic and electrocaloric applications.

II. EXPERIMENT

Preparation of $(Pb_{1-x}La_x)(Zr_{0.52}Ti_{0.48})O_3$ ceramic targets: $(Pb_{1-x}La_x)(Zr_{0.52}Ti_{0.48})O_3$ ceramic targets with at. % of La varying as 0%, 0.1 %, 0.5% and 1% were fabricated using standard solid state processing technique. All chemicals (Alfa Aesar) were used as received with a minimum assay of 99.99 %. Stoichiometric amounts of zirconium dioxide (ZrO_2) and titanium dioxide (TiO_2) powders were mixed in a mortar and pestle, and then the powder mixture was ball-milled in ethanol for 24 hrs using 5 mm ZrO_2 grinding media. The slurry was dried in an oven at 120°C, and the powder mixture was reground in mortar and pestle and sieved through 200 μm mesh. The sieved powder was placed in an alumina (Al_2O_3) crucible and calcined in the furnace at 1300°C for 4 h. The calcined powder was divided into four parts to prepare PLZT targets with different compositions. At this stage, 30 at. % excess PbO was added to each mixture and the powder mixtures were again ball milled, dried, and sieved. The excess PbO was added to compensate for the Pb loss during laser ablation. One part of the mixture was used to prepare the undoped PZT target. The other three parts were mixed with required stoichiometric amounts of lanthanum dioxide (La_2O_3) to prepare PLZT targets with varying at. % of La. The prepared powder mixtures were again ground in mortar and pestle and ball-milled in ethanol for 24 h. After that, slurries were dried in the oven at 120°C, ground, placed in Al_2O_3 crucibles and calcined at 950°C for 2 h. The ball-milling, drying and grinding procedure was repeated to ensure the homogeneous distribution of the La in the prepared targets. The resulting powder mixtures were then cold-pressed into cylindrical pellets (dimensions of 1" diameter and 0.5" thickness) using stainless-

steel die-punch assembly. Finally, the pellets were sintered at 800°C for 30 min to fabricate the PLZT targets.

In-situ fabrication of PLZT thin film capacitors using pulsed laser deposition (PLD): PLZT thin films capacitors using LSMO top/bottom electrodes were fabricated on single-crystal STO (100) and STO (111) substrates using PLD. The details of the deposition parameters for the optimized growth of PZT/LSMO thin films have been reported earlier [49]. Briefly, a high purity (99.9 % pure) ceramic target of stoichiometric $\text{La}_{0.7}\text{Sr}_{0.3}\text{MnO}_3$ (Kurt J. Lesker Company) and an as-prepared PLZT target, were ablated in sequence using a KrF excimer laser ($\lambda = 248$ nm, frequency 10 Hz) with fluences of 2 and 3 J/cm² at the target surface, respectively. The deposition chamber was equipped with a multi-target carousel that allowed for the *in-situ* deposition of multilayers with clean interfaces. A distance of 6 cm was maintained between the substrate and the targets during the depositions. In the optimized synthesis process, initially a 100 nm thick epitaxial thin film of LSMO was deposited on each of 0.5 x 1 cm² STO (100) and STO (111) substrates kept under the same conditions at 750 °C under an ambient oxygen pressure (pO₂) of 10 mTorr. This initial LSMO layer acted as the bottom electrode during the polarization of the PLZT thin films. The subsequent PLZT layer was deposited at 550 °C under a pO₂ of 500 mTorr with a thickness of 300 nm. A shadow mask was used during the PLZT layer deposition to preserve an open access to the LSMO bottom electrode. After the PLZT layer deposition, top LSMO electrodes of 100 μm in diameter and 50 nm thickness were deposited using a shadow mask at 550 °C under a pO₂ of 10 mTorr. After deposition, the PLD chamber was flooded with pure oxygen (500 mTorr) and the samples were gradually cooled down to room temperature (approx. 2 h). For comparison, undoped $\text{Pb}(\text{Zr}_{0.52}\text{Ti}_{0.48})\text{O}_3$ thin films were also grown under the same conditions.

Characterizations: The phase purity, crystalline quality and degree of texturing in the PLZT thin films were characterized by x-ray diffraction (XRD) with a Bruker AXS D8 diffractometer equipped with high-resolution Lynx Eye position-sensitive detector using Cu K α radiation ($\lambda = 1.5418\text{\AA}$). The in-plane epitaxy was determined from XRD azimuthal (\square) scans using a Philips X'pert diffractometer equipped with a 3D goniometer. High resolution reciprocal space maps (RSM) were acquired with a Panalytical PW3050/65 X'Pert PRO HR diffractometer using 4-bounce primary monochromator on the incident beam (leaving only Cu-K α 1, $\lambda=1.54098\text{\AA}$) and a 3-bounce analyzer crystal before the proportional point detector. The surface morphologies were observed using an Atomic Force Microscope (AFM) (Digital Instruments III). The interfacial microstructure in the PLZT/LSMO thin films was analyzed using high resolution transmission electron microscopy (HRTEM) (FEI Tecnai F 20 S-Twin TEM). The sample for cross-sectional TEM analysis was prepared by milling a $5\text{ }\mu\text{m} \times 10\text{ }\mu\text{m}$ rectangular strip that was 100 nm in thickness from the film surface using a focused ion beam (FIB) (JOEL 4500 FIB/SEM) and Pt-welding it to a Cu TEM grid. Energy dispersive spectroscopy (EDS) attached to the TEM was used for compositional analysis.

Ferroelectric Polarization Measurements: The polarization measurements of the fabricated PLZT thin-film (using LSMO top/bottom electrodes) capacitors were performed at different temperature using a commercial Precision LC Ferroelectric tester (from Radiant Technologies, Inc) equipped with a micro-probe station. During the hysteresis measurements, a constant standard bipolar input profile was used at 100 ms period but varying the driving voltages from 1 V to 9 V. The leakage current densities (J_L) in the PLZT thin-film capacitors were also measured by applying a stress voltage of 9 V for a period of 1s (soak time). The polarization-electric field (P-E) loops were collected independently from several (> 20) top

LSMO electrodes were found to be consistent. Repeatability of the polarization values were confirmed using a second series of PLZT thin films grown under the same conditions from the original targets (after polishing and cleaning their surfaces to get rid of any post-ablation surface irregularities). The ferroelectric hysteresis loops reported here have been corrected for contributions from leakage currents.

III. RESULTS AND DISCUSSION

Henceforth in the text, $(\text{Pb}_{1-x}\text{La}_x)(\text{Zr}_{0.52}\text{Ti}_{0.48})\text{O}_3$ (PLZT) thin films with at. % of La varying as 0 %, 0.1 %, 0.5 % and 1 % will be denoted as undoped PZT, 0.1 at. % PLZT, 0.5 at. % PLZT and 1.0 at. % PLZT, respectively.

A. Crystallinity and orientation

The single crystalline natures of the PLZT thin films grown on STO (100) and STO (111) substrates are evidenced from the XRD θ - 2θ patterns shown in Figs. 1 (a) and (b), respectively. In all cases, only strong (00 l) ($l = 1, 2$ and 3) and (l ll) diffraction peaks of the tetragonal PZT phase (JCPDS 01-070-4060) are observed along with the (l 00) ($l = 1, 2$, and 3) and (l ll) peaks of the pseudo-cubic perovskite LSMO phase (JCPDS 01-089-4461) and the single-crystal STO (100) and (111) substrates (in Figs. 1(a) and (b), respectively); indicating the high quality epitaxial growth of the films in both (001) and (111) orientations [49]. No secondary phase formations are observable within the resolution limits of the instrument. The small lattice mismatch between LSMO (pseudo-cubic perovskite, $a = 3.87 \text{ \AA}$) and the STO (cubic perovskite, $a = 3.905 \text{ \AA}$) substrate allowed for their epitaxial growth and the close proximity of their XRD peaks as shown in the insets to Figs.1(a) and (b) [56-59].

Azimuthal (\square) scans were performed about the PZT (101) crystallographic planes to confirm the in-plane epitaxial relationships of the PLZT (001) and PLZT (111) films. Fig. 1(c)

shows a representative ω -scan pattern; the occurrence of peaks at regular intervals of 90° is a consequence of the four-fold cubic symmetry of the PLZT layer in the PLZT (001) films. Rocking curves (ω -scans) performed about the PZT (002) crystallographic planes for undoped PZT and 1.0 at. % PLZT films shown in Fig. 1(d) yield peaks with a narrow full-width at half-maxima (FWHM) ($0.7^\circ \leq \Delta\omega \leq 0.8^\circ$) values, confirming the excellent out-of-plane orientation of the PLZT (001) layers.

Figure 1 (e) shows the characteristic Raman spectra of the (001) (or c -axis) oriented epitaxial PLZT (001) films. As typically observed in epitaxial thin films and nanostructures of the tetragonal PZT phase, a distinct splitting between the E(TO) and A_1 (LO) Raman modes and broadening of the peaks is noticeable in all the PLZT films [60-62]. In all cases, isolated broad peaks corresponding to A_1 (1TO), E(3TO+2LO) i.e. E(silent) + B_1 , E(4TO), and A_1 (3LO) Raman modes are observed that match with those reported for epitaxial $\text{PbZr}_{0.52}\text{Ti}_{0.48}\text{O}_3$ (001) thin films in their FE phase [63,64]. The observed features indicate that our PLZT films are virtually single phase. From Fig. 1 (e) a slight shift of the E(4TO) peaks to lower frequency is observed (indicated by red dotted arrow) as the La doping increased from 0 to 0.5 at. % in the PLZT films while the E(3TO+2LO) peak positions remain unchanged (indicated by blue dotted line). This could possibly indicate a lattice distortion of the PZT unit cell induced by La incorporation in the PLZT films. This can be speculated since similar peaks shift in the Raman spectra have been previously attributed to the tetragonal lattice distortion of PZT in Nd-doped PZT thin film [65].

B. Lattice distortion of PLZT unit cell

Figures 2 (a) and (b) show the XRD symmetric θ - 2θ scans near the PZT (002) and PZT (111) planes in PLZT (001) and PLZT (111) thin films, respectively. A distinct shift of the XRD peaks to lower 2θ values (dotted arrows in Figs. 2 (a) and (b)) is observed in both PLZT (001)

and (111) films as the La doping increases from 0 at. % to 0.5 at. % with respect to the unchanging substrate peaks position for STO (100) and STO (111). In both (001) and (111) orientations, no peak shift is observed for 1.0 at. % PLZT with respect to the undoped PZT sample. It is also noted that there is a distinct peak broadening as the doping concentration increases, which could be associated with formation of smaller crystalline sizes in the PLZT films as compared to the undoped PZT films. From Fig. 2 it can be inferred that an increase in the out-of-plane lattice parameters occur in both PLZT (001) and (111) films as the La concentration increases from 0 to 0.5 at. %. On the other hand, asymmetric 2θ - ω scans about the PZT (111) planes in PLZT (001) films as shown in Fig. 2 (c) exhibit a large shift in XRD peaks to higher 2θ values as the La doping increases from 0 to 0.5 at. %, and again no peak shift for 1 at. % PLZT film. Similar peak shifts to higher 2θ values as the La doping increased from 0 to 0.5 at. % were observed in the PLZT (111) films (see Supplemental Material, Figure S1) [66]. These results were confirmed from the symmetric scans about PZT (001) and (003) planes, and asymmetric scans about PZT (101), (110), and (211) planes, respectively (not shown here). It is to be noted that the PZT planes for the asymmetric scans were carefully chosen such that there were no contributions to the XRD peaks from the underlying LSMO or STO layers.

The lattice parameters (a and c) of the tetragonal PLZT unit cell were calculated for both PLZT (001) and PLZT (111) films from the detailed XRD symmetric and asymmetric scans, respectively. Table 1 summarizes the lattice parameters and tetragonality for PLZT films in (001) and (111) orientations. We mention here that the lattice parameters for the pseudo-cubic LSMO layers ($c = 3.887 \pm 0.003 \text{ \AA}$ and $a = 3.897 \pm 0.003 \text{ \AA}$) in all the samples were found to be very close to that of the underlying single-crystal STO substrates (as seen in the unchanging peak positions of LSMO (111) peaks in Fig. 2 (b)) [56,57]. The in-plane strain ($\epsilon_{||}$) and out-of-plane

strain (ε_{\perp}) for the undoped PZT film were calculated using the formula $\varepsilon = (a - a_o)/a_o$ where a is the in-plane ($a_{||}$) and out-of-plane (a_{\perp}) lattice parameters of the film (Table 1) and a_o is the in-plane (a or $a_{o||} = 4.055 \text{ \AA}$) and out-of-plane (c or $a_{o\perp} = 4.110 \text{ \AA}$) lattice parameters of undoped PZT bulk single crystals (JCPDS 01-070-4060), respectively. The undoped PZT layer experienced a minute in-plane compressive ($\varepsilon_{||} = -0.44\%$) and an extremely small out-of-plane tensile ($\varepsilon_{\perp} = 0.12\%$) strain, respectively. Due to this the undoped PZT unit cell experienced a slightly higher tetragonality of $c/a = 1.019$ (Table 1) as compared to that of the undoped PZT bulk crystals of $c/a = 1.013$. However, as can be seen in Table 1, in the 0.1 at.% and 0.5 at.% PLZT thin films the tetragonality was even higher than that of the undoped PZT film due to the substitution of La ion for Pb ion in the PLZT unit cell. In Fig. 2 (d), we plot the c , a and tetragonality (c/a) values for PLZT (001) and PLZT (111) unit cells as a function of La concentration. From Fig. 2 (d) it is clearly observed that the c values monotonically increase while the a values correspondingly decrease as La concentration increases from 0 to 0.5 at. % (see Table 1). This causes a large increase in the tetragonality (c/a) of the PLZT unit cell with respect to the undoped PZT unit cell. For 0.5 at. % PLZT (001), the tetragonality ($c/a = 1.03$) is almost 2 % higher than that of undoped PZT as can be seen in Fig. 2 (d). A systematic decrease in the unit cell volume is observed in 0.1 to 0.5 at. % PLZT as compared to the undoped PZT in both (001) and (111) crystallographic directions. This is consistent with the earlier report where the cell parameters of the undoped PZT thin film decreased with the addition of La dopant due to the substitution of the A-site in ABO_3 -type PZT unit cell with the La^{3+} ion having smaller radii than the Pb^{2+} ion [40]. However, as shown in Fig. 2 (d) when the La concentration is increased to 1.0 at. %, there is drastic reduction in the tetragonality in both PLZT(001) and PLZT (111) films (see Table 1). This probably indicates that with increased dopant concentration, not all the

dopants can occupy substitutional sites but some are restricted to the interstitial sites and grain boundaries, which could mitigate the tetragonality.

Further confirmation of unit-cell parameters for PLZT (001) thin films grown on LSMO/STO (100) substrates was obtained from high-resolution XRD reciprocal space maps (RSMs) using asymmetrical reflections. Figure 2 (e) shows a representative RSM performed about the STO (103) peak for the 0.5 at. % PLZT thin film. Single peaks corresponding to LSMO (103) and PLZT (103) reflections are observed near the STO substrate peak, certifying the epitaxial growth of both layers. While the LSMO film peak is very close to STO -as expected given their structural similarity- the position of the PLZT peak indicates a clear structural relaxation due to the larger lattice parameters of PLZT. Similar RSMs were obtained for PLZT (001) thin films at varying La concentrations (see Supplementary Information, Figure S2) [66]. The out-of-plane (*c*) and in-plane (*a*) lattice parameters and the tetragonality (*c/a*) in the PLZT (001) films as calculated from the RSMs (see Supplementary Information, Figure S2) show the same trend as those obtained from XRD symmetric and asymmetric scans shown in Figure 2 (d) [66].

In summary, from the above extensive XRD analyses it is confirmed that substitutional doping of La in Pb sites increases the tetragonality in the PLZT unit cell irrespective of the crystal orientation, as evident in both PLZT (001) and PLZT (111) thin films. The enhanced tetragonality with increasing La doping concentration is evident in the undoped PZT, 0.1 at. % PLZT, and 0.5 at. % PLZT thin films. However, further increase in La doping concentration reduces the tetragonality in PLZT films as seen in the 1 at. % PLZT thin films; which possibly could arise when not all of the La ions substitute Pb ions, but several occupy interstitial sites or precipitates at grain boundaries. Nonetheless, since the specific composition of $\text{PbZr}_{0.52}\text{Ti}_{0.48}\text{O}_3$

(PZT) in this case is near its morphotropic phase boundary (MPB), even such small changes (1-2 %) in the tetragonality of the PZT unit cell due to La-doping could have profound effect on its FE properties [66].

C. Interfaces

Cross-sectional microstructure of the PLZT thin films revealed sharp and flat interfaces with uniform thicknesses of the individual layers, as illustrated in the representative TEM image for the 0.5 at. % PLZT (001) thin film in Fig.3 (a). From the figure, indications of an out-of-plane columnar structure can be observed in the PLZT (001) layer which is consistent with the c-axis growth of PLZT (as seen in the XRD analysis in Fig.1). The HRTEM image of the PLZT-LSMO interface in Fig. 3 (b) (as captured from a region marked with red dotted box in Fig. 3 (a)) shows atomically sharp and flat phase-boundaries with continuous lattice fringes from the bottom LSMO layer to the top PLZT layer. This clearly demonstrates the single crystalline nature and the cube-on-cube epitaxial growth morphology of the PLZT film. Similar HRTEM images captured at different locations along the PLZT-LSMO interface showed no evidence of any structural defects such as lattice misfits or twin planes. The measured d_{001} -spacing values for PLZT ($d = 0.391$ nm) and LSMO ($d = 0.389$ nm) in Fig.3 (b) are consistent with those obtained from the XRD analysis. HRTEM images of the bottom LSMO-STO interface also showed single-crystalline growth with no structural defects as depicted in our earlier report [68]. The HRTEM image in Fig. 3 (c) exhibits the single-crystalline defect-free growth of the PLZT layer as captured from a region marked with blue dotted box in Fig. 3 (a) and away from the PLZT-LSMO interface. The measured d_{001} -spacing value for PLZT is same as that obtained near the interface. The (001) and (100) crystallographic directions in the PLZT film have been marked with white arrows. EDS spectrum captured near this region of the PLZT layer (during TEM

analysis) exhibited distinct peaks from the dopant La and the constituent elements (viz. Pb, Zr, Ti, and O) of PZT, confirming the presence of La in the PLZT layer (see Supplementary Information, Figure S3). The micro-crystallinity in the samples was determined from selected area electron diffraction (SAED) patterns captured at different regions along the interfaces and the individual layers. Figures 3(d) and (e) show the SAED patterns captured near the PZT-LSMO interfaces for the 0.5 at. % PLZT (001) film and the undoped PZT film, respectively. The linear dotted single-crystalline SAED pattern in Fig.3 (d) shows the tetragonal symmetry (marked by white box and arrow pointing towards the *c*-axis) and the close in-plane lattice parameters of the PLZT and LSMO layers in the 0.5 at. % PLZT film. In comparison, the SAED pattern obtained near the undoped PZT-LSMO interface shows the presence of slightly-displaced in-plane lattice planes, as shown by red and yellow arrows in Fig. 3 (e), indicating a lattice mismatch between the undoped PZT and LSMO layers. Further, from the marked white boxes in Figs.3 (d) and (e), the enhanced tetragonality in the PLZT film can be observed as compared to the undoped PZT film. From the SAED patterns in Figs.3 (d) and (e), the tetragonality ratio for the 0.5 at. % PLZT layer was calculated to be $c/a \approx 1.04$ and that for the undoped PZT layer was $c/a \approx 1.02$, consistent with those obtained from the XRD analyses. From the TEM analysis it is concluded that the PLZT layer and the LSMO layer have almost identical lattice parameters near the interface in the 0.5 at. % PLZT sample. On the other hand, undoped PZT and LSMO have slightly mismatched lattice parameters with strain-relaxed undoped PZT unit cell having larger lattice parameter than the underlying LSMO layer. Figure 3 (f) shows a typical AFM image of the PLZT layer exhibiting smooth particulate-free surface with low roughness ($R_{\text{rms}} \sim 4$ nm) and uniform grains of sizes $\sim 170 \pm 10$ nm (consistent with the high quality growth of the PLZT layer). The distinct grain growth on the PLZT surfaces suggest a relaxation of the epitaxial strain

in the 300 nm thick PLZT layer which was also evident in the XRD RSM in Fig. 2 (e) earlier. Typically, such thin film growth takes place via the nucleation, growth and coalescence of epitaxially oriented islands, and result in neighbouring grains having similar crystallographic orientations. These results are thus consistent with those obtained from the XRD analysis. Thus, from the XRD, AFM and HRTEM analyses, it can be inferred that the PLZT films are relaxed that the observed differences in lattice parameters in the PLZT thin films are solely due to the doping of La onto the Pb sites in the PLZT unit cell. This leads to the conclusion that La-doping rather than strain leads to enhanced tetragonality in these epitaxial PLZT thin films.

D. Ferroelectric properties

Polarization vs. electric field (P - E) curves measured at varying driving voltages from 1 V to 9 V for PLZT (001) films showed well-saturated, square and highly symmetric hysteresis loops above a nominal switching voltage of 3 V (see Supplementary Information, Figure S4). While both the saturation polarization (P_s) and remanent polarization (P_r) consistently increase with increasing driving voltages, the coercive fields (E_c) show almost constant values indicating negligible effects from charged defects or space-charges in these samples, which is typically observed in PZT thin films [69,70,71,72]. Leakage current density vs. voltage (J_L - V) characteristics for the PLZT films exhibited almost two orders of magnitude lower values of leakage currents through the PLZT capacitors as compared to those reported earlier (see Supplementary Information, Figure S5) [73]. Such excellent FE properties in PLZT thin films can be attributed to the high quality single-crystalline nature of the samples and the defect-free nature of their interfaces, as observed earlier in their XRD and TEM analysis (Figs. 1 and 3), respectively. The P - E curves for the 0.1 at. % and 0.5 at. % PLZT (001) thin films (see

Supplementary Information, Figure S4)) show higher P_{sat} and P_r values than the undoped PZT thin film at all driving voltages.

To clearly demonstrate the enhanced FE properties of PLZT thin films at lower La-doping concentrations, the P - E curves for all the PLZT and undoped PZT thin films for both (001) and (111) directions (measured at the 9 V) are shown in Figs. 4 (a) and (b), respectively. The schematic diagrams in the insets to Figs. 4 (a) and (b) depict the top-bottom electrode and thin film symmetric capacitor geometries used in the polarization measurements. It is noted from the schemes that the polarization direction for PLZT (001) and PLZT (111) are along the [001] and [111] directions of the PLZT unit cell since the electric field is applied in the out-of-plane direction. Table 1 summarizes the polarization values for PLZT thin films in both (001) and (111) orientations. The P_r value for the undoped PZT (001) film of $49(\pm 2) \mu\text{C}/\text{cm}^2$ at E_c of $39(\pm 3) \text{ kV}/\text{cm}$ matches well with earlier reports on epitaxial PZT (001) films (with the same composition of PZT as here)[74]. Reported P_r values in PZT vary from 15 to $36 \mu\text{C}/\text{cm}^2$ (at E_c range of 40 to 194 kV/cm) for polycrystalline PZT films and with higher P_r values of 45 to 54 $\mu\text{C}/\text{cm}^2$ (at E_c range of 35-40 kV/cm) recorded for epitaxial PZT thin films[6,31,45,49,54]. From Fig. 4 (a), it is observed that compared to the undoped PZT (001) film, the P_r values in the PLZT films progressively increase from $60 \mu\text{C}/\text{cm}^2$ for 0.1 at. % PLZT to as high as $91 \mu\text{C}/\text{cm}^2$ for 0.5 at. % PLZT (i.e. almost two times than that of the undoped PZT film). However, at higher La doping of 1.0 at. % PLZT, the P_r value is actually lower than that in the undoped PZT film (see Table 1). A similar trend in polarization characteristics is observed in PLZT (111) films as in Fig. 4 (b), with increasing P_r values with La concentration for 0.1 and 0.5 at. % PLZT films as compared to the undoped PZT film. We observe that the P_r values in PLZT (111) films are much lower than those in PLZT (001) films at all doping concentrations, since in the tetragonal PZT

unit cell the [111] direction is the hard axis of polarization[74].It is noted that the observed trend in polarization values in PLZT thin films with increasing La concentrations is comparable to that reported in a parallel system of donor-type Nb-doped PZT thin films (see Supplemental Material, Figure S6) [66,75]. From the plot of E_c values for PLZT (001) and (111) films as a function of La concentrations (see Supplemental Material, Figure S6), it is clear that the E_c values decrease monotonically with La concentration as reported in bulk PLZT ceramics[27,29,34-37,66]. We infer that with increasing La doping concentrations, the densities of $(La_{Pb}^{\bullet} - V_{Pb}^{//})$ -type defect dipoles increase within the PLZT unit cell. The different local environments created as a result of these spatially-dispersed defect dipoles may affect the domain wall motion in PLZT. The interaction of these randomly oriented defect dipoles with each other and the polarization vector of the PLZT unit cell could possibly assist domain switching at lower fields; consequently, leading to lower E_c values.

E. Correlation of polarization with crystal lattice distortion

In order to understand the enhanced FE properties observed in the PLZT thin films, we looked into the correlation between the remanent polarization and the crystal lattice distortion in the epitaxial PLZT thin films. From Table 1 it is observed that under varying La concentrations PLZT thin films have different tetragonality(c/a)and associated P_r values. The difference in the lattice parameters c and a values is the measure of the lattice distortion ($c/a - 1$) in the tetragonal PLZT unit cell. Using the Landau-Ginsburg-Devonshire type thermodynamic model, it is known that the spontaneous polarization (P_s) induced by the lattice distortion of a FE unit cell is related by: [76]

$$QP_s^2 = c/a - 1, \quad (1)$$

where Q is the electrostrictive coefficient (in standard notation). In our case, (1) can be modified to the following:

$$QP_r^2 = c/a - 1, \quad (2)$$

since P_r is the macroscopic measurement of P_s for a defect-free tetragonal PLZT film. Using the structural and ferroelectric data from Table 1, we plotted the square of the P_r versus the lattice distortion ($c/a - 1$) for the different La doping concentrations as shown in Figure 5 (a) for PLZT (001) and PLZT (111) films. A quasi-linear relationship is observed and from the slopes of the linear fits of the data, the Q_{001} value was calculated to be $0.072 (\pm 0.005) \text{ m}^4/\text{C}^2$ and Q_{111} value was calculated to be $0.069 (\pm 0.004) \text{ m}^4/\text{C}^2$. The Q_{001} and Q_{111} values are close to each other since the compositions of PLZT films are same in both orientations. However, the electrostrictive coefficient in PLZT films are higher than that reported by Morioka et al. ($Q = 0.049 \text{ m}^4/\text{C}^2$) for c -axis oriented undoped PZT (001) thin films[77]. The calculated Q value in our case is indeed very close to that of the reported theoretical value, $Q_{11} = 0.089 \text{ m}^4/\text{C}^2$ in single-crystal PbTiO_3 [78]. The excellent agreement of the experimental data with the theoretical values and the higher Q values observed in the PLZT films demonstrate the enhanced polarization behaviour in PLZT as a result of lattice distortion with incorporation of La in PZT. The estimated P_s value in the 0.5 at. % PLZT (001) film ($P_s \approx 91 \text{ } \mu\text{C}/\text{cm}^2$) is higher than the theoretical value ($P_s = 70 \text{ } \mu\text{C}/\text{cm}^2$) calculated for undoped PZT single crystals[79]. It has been reported that higher tetragonality (as high as 1.06) can lead to even higher P_s value ($P_s = 110 \text{ } \mu\text{C}/\text{cm}^2$) which was reported by Vrejoiu et al. for epitaxial PZT thin films with different compositions ($\text{PbZr}_{0.2}\text{Ti}_{0.8}\text{O}_3$) than in our case[80]. Since the P_s value in PZT decreases as the composition reaches the MPB,[69] it is expected that our values are lower than those reported by Vrejoiu et al.[80] since our PZT composition is near the MPB. Morioka et al.[77] also showed the

relationship between P_s and $(c/a - 1)$ for tetragonal PZT over a wide range of PZT compositions. From the corresponding curve (as shown in Figure 5 of their paper)[77], a tetragonality of 1.034 as in our 0.5 at. % PLZT film (see Table 1) would result in a theoretical maximum P_s of $\approx 97 \mu\text{C}/\text{cm}^2$ which is very close to our reported value ($P_s \approx 91 \mu\text{C}/\text{cm}^2$) for the specific PZT composition in this work.

From the foregoing arguments, it can be summarized that low La substitution in tetragonal PZT thin films results in lattice distortion and enhanced tetragonality of the PLZT unit cell. This consequently creates a larger displacement of the Pb^{2+} ions with respect to the body-center of the perovskite PLZT unit cell as compared to the undoped PZT cell, as shown schematically in Fig. 5(b); consequently, enhancing its spontaneous polarization. The enhanced spontaneous polarization under the application of an external applied electric field (E) (shown by thick red arrow) manifests itself macroscopically as enhanced remanent polarization, as recorded in these epitaxial PLZT thin films. Since the solubility of La in bulk PZT for a composition near its MPB (as in this case) is as low as a few atomic percent (< 2 at. %), slight excess La doping could result in the precipitation of mixed phases such as $\text{La}_2\text{Zr}_2\text{O}_7$ and $\text{La}_2\text{Ti}_2\text{O}_7$, which could be detected using XRD in bulk samples[1]. However, in these epitaxial PLZT thin films micro-precipitates resulting from any excess La doping was undetected even in the 1 at. % PLZT sample within the resolution limits of the XRD. On the contrary, cross-sectional HRTEM image captured near the PLZT-LSMO interface for the 1 at. % PLZT film showed possible indication of nano-sized precipitates of secondary impurity phases as shown in the Supplementary Material (Figure S7) which could be associated with excess La doping in the 1 at. % PLZT thin film. The SAED pattern captured near the PLZT-LSMO interface for the 1 at. % PLZT thin film as shown in the Supplementary Material (Figure S7) clearly shows single crystalline growth. The red and

yellow thick arrows in Figure S7b indicate the mismatched lattice parameters of 1 at. % PLZT and LSMO. layers. Comparing the SAED patterns for the undoped PZT (Figure 3e) and the 1 at. % PLZT (Figure S7) thin films reveal their similar tetragonality as also evidenced in the XRD analyses.

IV. CONCLUSIONS

We report on the enhanced polarization observed in tetragonal PLZT thin films as a result of low La doping. Both (001) and (111) oriented epitaxial PLZT thin film capacitors were fabricated using the conducting oxide LSMO as the top and bottom electrodes on lattice-matched STO substrates under optimized growth conditions in PLD technique. Detailed investigation on the structural and FE properties reveal enhance tetragonal distortion and dramatic improvement in FE polarization in the PLZT films as compared to undoped PZT irrespective of their orientations. Since the films are relaxed at 300 nm thicknesses, the enhanced properties are solely due to the La doping in PLZT rather than strain. Symmetric hysteresis loops with record high remanent polarizations of $91 \mu\text{C}/\text{cm}^2$ at 9 V applied voltage were achieved in 0.5 at. % PLZT (001) thin film which exceed all previously published values in PLZT thin films. The experimental data match well with the theoretical model for lattice-distortion induced change in spontaneous polarization in PLZT unit cell. With the results presented here we have empirically shown that the remanent polarization can be increased drastically at reduced coercive fields in PZT via low La doping. The understanding of such property enhancements via doping induced crystal distortion could be used in the design of new PZT-based FE devices with superior property coefficients and functionalities. Such high remanent polarization as observed in our PLZT thin films could be of potential advantage for data storage and electrocaloric applications.

ACKNOWLEDGEMENTS

This work was partially supported by the Florida Cluster for Advanced Smart Sensor Technologies (FCASST) under the Florida State University System Board of Governor's "New Florida 2010" Initiative and the United States Army (Grant No. W81XWH1020101/3349). DM acknowledges the funding from the Technical Research Center, Department of Science and Technology, Government of India. JJ and DG additionally acknowledge the US Department of the Army (Grant No. W911NF-09-1-0435). DP acknowledges the Beatriu de Pinós postdoctoral fellowship BP-DGR 2014 from Agència de Gestió d'Ajuts Universitaris i de Recerca (AGAUR). We thank Akito Sakata for assistance in the preparation of PLD targets. We thank Xavier Moya for his helpful comments on the paper.

Supplemental Material

See Supplemental Material at [URL will be inserted by publisher] for [XRD asymmetric 2θ - ω scans, reciprocal space maps and EDS spectrum, voltage dependent polarization and leakage current density of PLZT thin films].

REFERENCES

- [1] G. H. Haertling, *J. Am. Ceram. Soc.* **82**, 797 (1999).
- [2] J. F. Scott, *Science* **315**, 954 (2007).
- [3] R. Guo, L. E. Cross, S. E. Park, B. Noheda, D. E. Cox, and G. Shirane, *Phys. Rev. Lett.* **84**, 5423 (2000).
- [4] J. F. Scott and C. A. P. Dearaujo, *Science* **246**, 1400 (1989).
- [5] S. Xu, B. J. Hansen, and Z. L. Wang, *Nat. Commun.* **1**, 93 (2010).
- [6] A. Datta, D. Mukherjee, C. Kons, S. Witanachchi, and P. Mukherjee, *Small* **10**, 4039 (2014).
- [7] D. Mukherjee, A. Datta, C. Kons, M. Hordagoda, S. Witanachchi, and P. Mukherjee, *Appl. Phys. Lett.* **105**, 212903 (2014).
- [8] N. Izyumskaya, Y. Alivov, S. Cho, H. Morkoc, H. Lee, and Y. Kang, *Crit. Rev. Solid State Mater. Sci.* **32**, 111 (2007).
- [9] H. Thomann, *Ferroelectrics* **4**, 141 (1972).
- [10] A. Datta, D. Mukherjee, S. Witanachchi, and P. Mukherjee, *Adv. Func. Mater.* **24**, 2638 (2014).
- [11] A. Datta, D. Mukherjee, M. Hordagoda, S. Witanachchi, P. Mukherjee, R. V. Kashid, M. A. More, D. S. Joag, and P. G. Chavan, *ACS Appl. Mater. Interfaces* **5**, 6261 (2013).
- [12] J. F. Scott, *Ferroelectric Memories*; Springer Series in Advanced Microelectronics; (Springer-Verlag Berlin Heidelberg GmbH: New York, 2000; Vol. 3, pp 248).
- [13] R. Waser, in *Nanoelectronics and Information Technology* (Wiley-VCH Verlag & Co. KGaA Weinheim, Germany, 2012, pp 1040).
- [14] R. Ramesh, and N. A. Spaldin, *Nat. Mater.* **6**, 21 (2007).

- [15] B. Jaffe, W. R. Cook and H. Jaffe, Piezoelectric ceramics, Academic Press, San Diego, CA, 1971.
- [16] A. Moure, A. Castro and L. Pardo, Aurivillius-type ceramics, a class of high temperature piezoelectric materials: drawbacks, advantages and trends, Prog. Solid State Chem., 37, 15-39 (2009).
- [17] D. Mukherjee, M. Hordagoda, P. Lampen, M. H. Phan, H. Srikanth, S. Witanachchi, and P. Mukherjee, Phys. Rev. B **91**, 054419 (2015).
- [18] A. S. Mischenko Q. Zhang, J. F. Scott, R. W. Whatmore, and N. D. Mathur, Science **311**, 1270 (2006).
- [19] R. Chukka, J. W. Cheah, Z. Chen, P. Yang, S. Shannigrahi, J. Wang and L. Chen, Appl. Phys. Lett. **98**, 242902 (2011).
- [20] W. Geng, Y. Liu, X. Meng, L. Bellaiche, J. F. Scott, B. Dkhil, and A. Jiang, Adv. Mater. **27** 3165 (2015).
- [21] W. G. Liu, B. Jiang, and W. G. Zhu, Appl. Phys. Lett. **77**, 1047 (2000).
- [22] D. J. Singh, M. Ghita, M. Fornari, and S. V. Halilov, Ferroelectrics **338**, 73 (2006).
- [23] P. Gonnard and M. Troccaz, J. Solid. State. Chem. **23**, 321 (1978).
- [24] W. Qiu and H. H. Hng, Mater. Chem. Phys. **75**, 151 (2002).
- [25] G. H. Haertling, Ferroelectrics **75**, 25 (1987).
- [26] G. H. Haertling and C. E. Land, J. Am. Ceram. Soc. **1971**, 54, 1-11.
- [27] M. Prabu, I. B. S. Banu, S. Gobalakrishnan, and M. Chavali, J. Alloys Comp. **551**, 200 (2013).
- [28] M. Narayanan, S. Tong, S. Liu, B. Ma, and U. Balachandran, Appl. Phys. Lett. **102**, 062906 (2013).

- [29] B. Ma, S. Liu, S. Tong, M. Narayanan, and U. Balachandran, *J. Appl. Phys.***112**, 114117 (2012).
- [30] W. Zhu, I. Fujii, W. Ren, and S. Trolier-McKinstry, *J. Am. Ceram. Soc.* **95**, 2906 (2012).
- [31] Q. Tan, Z. Xu, and D. Viehland, *Philos. Mag. B***80**, 1585 (2000).
- [32] X. Dai, Z. Xu, and D. Viehland, *Phil. Mag. B* **70**, 33 (1994).
- [33] A. A. Bokov and Z. G. Ye, *J. Mater. Sci.* **41**, 31 (2006).
- [34] A. Pramanick, D. Damjanovic, J. E. Daniels, J. C. Nino, and J. L. Jones, *J. Am. Ceram. Soc.***94**, 293 (2011).
- [35] R. Gerson, *J. Appl. Phys.***31**, 188 (1960).
- [36] G. Rossetti, M. Rodriguez, A. Navrotsky, L. Cross, and R. Newnham, *J. Appl. Phys.***77**, 1683 (1995).
- [37] K. Wojcik, *Ferroelectrics***99**, 5 (1989).
- [38] G. Rossetti, L. Cross, and J. Cline, *J. Mater. Sci.***30**, 24 (1995).
- [39] C. A. Randall, G. A. Jr. Rossetti, and W. Cao, *Ferroelectrics***150**, 163 (1993).
- [40] Y. H. Son, K. T. Kim, and C. I. Kim, *J. Vac. Sci. Technol. A***22**, 1743 (2004).
- [41] K. B. Han, C. H. Jeon, H. S. Jhon, and S. Y. Lee, *Thin Solid Films***437**, 285 (2003).
- [42] I. Stolichnov, A. Tagantsev, N. Setter, J. S. Cross, and M. Tsukada, *Appl. Phys. Lett.***74**, 3552 (1999).
- [43] I. Boerasu, L. Pintilie, and M. Kosec, *Appl. Phys. Lett.***77**, 2231 (2000).
- [44] H. H. Park, H. H. Park, and R. H. Hill, *Appl. Surf. Sci.***237**, 427 (2004).
- [45] B. Ma, S. Chao, M. Narayanan, S. Liu, S. Tong, R. E. Koritala, and U. Balachandran, *J. Mater. Sci.***48**, 1180 (2013).

- [46] K. Uchiyama, T. Shiosaki, T. Kosaka, A. Kasamatsu, M. Echizen, *Ceram. Int.***34**, 979 (2008).
- [47] G. L. Brennecka and B. A. Tuttle, *J. Mater. Res.***22**, 2868(2007).
- [48] M. Okada and K. Tominaga, *J. Appl. Phys.***71**, 1955 (1992).
- [49] D. Mukherjee, R. Hyde, M. Hordagoda, N. Bingham, H. Srikanth, S. Witanachchi, and P. Mukherjee, *J. Appl. Phys.***112**, 064101 (2012).
- [50] G. Tyrrell, T. York, L. Coccia, and I. Boyd, *Appl. Surf. Sci.* **96**, 769(1996).
- [51] D. Mukherjee, R. Hyde, P. Mukherjee, H. Srikanth, and S. Witanachchi, *J. Appl. Phys.***111**, 089905 (2012).
- [52] N. D. Scarisoreanu, F. Craciun, A. Andrei, V. Ion, R. Birjega, A. Moldovan, M. Dinescu, C. Galassi, *Thin Solid Films* **541**, 127(2013).
- [53] M. Gaidi, A. Amassian, M. Chaker, M. Kulishov, and L. Martinu, *Appl. Surf. Sci.***226**, 347(2004).
- [54] K. S. Liu, Y. J. Chen, G. Jamn, I. N. Lin, *Appl. Phys. Lett.***75**, 2647(1999).
- [55] W. B. Wu, K. H. Wong, C. L. Choy, Y. H. Zhang, *Appl. Phys. Lett.* **77**, 3441(2000).
- [56] D. Mukherjee, N. Bingham, M. Hordagoda, M. H. Phan, H. Srikanth, S. Witanachchi, and P. Mukherjee, *J. Appl. Phys.***112**, 083910(2012).
- [57] F. Yang, N. Kemik, M. D. Biegalski, H. M. Christen, E. Arenholz, and Y. Takamura, *Appl. Phys. Lett.* **97**, 092503 (2010).
- [58] F. Tsui, M. C. Smoak, T. K. Nath, and C. B. Eom, *Appl. Phys. Lett.***76**, 2421(2000).
- [59] M. Izumi, Y. Konishi, T. Nishihara, S. Hayashi, M. Shinohara, M. Kawasaki, Y. Tokura, *Appl. Phys. Lett.***73**, 2497 (1998).
- [60] G. Burns and B. A. Scott, *Phys. Rev. Lett.* **25**, 1191 (1970).

- [61] C. M. Foster, Z. Li, M. Grimsditch, S. K. Chan, and D. J. Lam, Phys. Rev. B **48**, 10160 (1993).
- [62] K. Nishida, M. Osada, S. Wada, S. Okamoto, R. Ueno, H. Funakubo, and T. Katoda, Jpn. J. Appl. Phys. **44**, 827 (2005).
- [63] M. G. Karkut, F. L. Marrec, C. Marechal, R. K. Steinseth, M. E. Marssi, R. Farhi, J. L. Dellis, and F. Portemer, Ferroelectrics **225**, 261 (1999).
- [64] S. H. Lee, H. M. Jang, H. H. Sung, and H. Yi, Appl. Phys. Lett. **81**, 2439 (2002).
- [65] J. Frantti, V. Lantto, and J. Lappalainen, J. Appl. Phys. **79**, 1065 (1996).
- [66] See Supplemental Material at [*URL will be inserted by publisher*] for x-ray asymmetric scan of PLZT (111) thin films; reciprocal space maps of PLZT (001) thin films at varying La doping concentrations, lattice parameters and tetragonality for PLZT (001) thin films as obtained from the reciprocal space maps; and variation of remanent polarization and coercive fields for PLZT thin films.
- [67] M. D. Nguyen, M. Dekkers, E. Houwman, R. Steenwelle, X. Wan, A. Roelofs, T. Schmitz-Kempen, and G. Rijnders, Appl. Phys. Lett. **99**, 252904(2011).
- [68] D. Mukherjee, N. Bingham, M. H. Phan, H. Srikanth, P. Mukherjee, S. Witanachchi, J. Appl. Phys. **111**, 07D730(2012).
- [69] J. F. Scott, Ferroelectrics. Rev. **1**, 1(1998).
- [70] J. J. Lee, C. L. Thio, and S. B. Desu, J. Appl. Phys. **78**, 5073(1995).
- [71] J. F. M. Cillessen, M. W. J. Prins, and R. M. Wolf, J. Appl. Phys. **81**, 2777 (1997).
- [72] S. Kim, H. Woo, J. Ha, C. Hwang, H. Kim, and A. Kingon, Appl. Phys. Lett. **78**, 2885(2001).

- [73] N. Kotova, Y. Podgorny, D. Seregin, A. Sigov, A. Vishnevskiy, and K. Vorotilov, *Ferroelectrics* **465**, 54 (2014).
- [74] J. Schwarzkopf and R. Fornari, *Prog. Cryst. Growth Character. Mater.* **52**, 159 (2006).
- [75] E. C. F. Souza, A. Z. Simoes, M. Cilense, E. Longo, and J. A. Varela, *Mater. Chem. Phys.* **88**, 155 (2004).
- [76] F. Jona and G. Shirane, *Ferroelectric Crystals* (Dover Publications, Inc.: 1993; pp 398).
- [77] H. Morioka, S. Yokoyama, T. Oikawa, H. Funakubo, and K. Saito, *Appl. Phys. Lett.* **85**, 3516 (2004).
- [78] M. J. Haun, E. Furman, S. J. Jang, H. A. McKinstry, L. E. Cross, *J. Appl. Phys.* **62**, 3331 (1987).
- [79] M. J. Haun, E. Furman, S. J. Jang, L. E. Cross, *Ferroelectrics* **99**, 63 (1989).
- [80] I. Vrejoiu, G. L. Rhun, L. Pintlilie, D. Hesse, M. Alexe, and U. Gösele, *Adv. Mater.* **18**, 1657 (2006).

TABLES

Table1. Structural and ferroelectric properties of $(\text{Pb}_{1-x}\text{La}_x)(\text{Zr}_{0.52}\text{Ti}_{0.48})\text{O}_3$ (PLZT) thin films grown in both [001] and [111] orientations with varying La concentrations as detailed in the text: lattice parameters (c and a), tetragonality (c/a), maximum polarization (P_{\max}), remanent polarization (P_r), and coercivity (E_c).

Sample	Orientation	Lattice parameters		Tetragonality	Polarization		
		c (Å)	a (Å)	c/a	P_{\max} ($\mu\text{C}/\text{cm}^2$)	P_r ($\mu\text{C}/\text{cm}^2$)	E_c (kV/cm)
Undoped PZT	[001]	4.115 ± 0.001	4.037 ± 0.002	1.019	53 ± 3	49 ± 2	39 ± 3
0.1 at. % PLZT	[001]	4.120 ± 0.002	4.020 ± 0.003	1.025	70 ± 2	60 ± 3	38 ± 2
0.5 at. % PLZT	[001]	4.128 ± 0.002	3.991 ± 0.004	1.034	103 ± 4	91 ± 4	36 ± 2
1.0 at. % PLZT	[001]	4.110 ± 0.003	4.057 ± 0.003	1.013	42 ± 4	36 ± 3	29 ± 1
Undoped PZT	[111]	4.089 ± 0.001	4.081 ± 0.002	1.002	34 ± 2	25 ± 3	35 ± 2
0.1 at. % PLZT	[111]	4.094 ± 0.002	4.075 ± 0.003	1.005	40 ± 2	28 ± 2	28 ± 3
0.5 at. % PLZT	[111]	4.102 ± 0.001	4.051 ± 0.005	1.013	54 ± 4	46 ± 4	22 ± 2
1.0 at. % PLZT	[111]	4.087 ± 0.003	4.082 ± 0.004	1.001	27 ± 3	20 ± 4	19 ± 4

FIGURE CAPTIONS

FIG. 1. Crystallinity and orientation in $(\text{Pb}_{1-x}\text{La}_x)(\text{Zr}_{0.52}\text{Ti}_{0.48})\text{O}_3$ (PLZT) thin films with varying La concentrations of 0 at. %, 0.1 at. %, 0.5 at. % and 1.0 at. %; denoted as undoped PZT, 0.1 at. % PLZT, 0.5 at. % PLZT and 1.0 at. % PLZT, respectively. XRD θ - 2θ patterns for PLZT thin films grown on (a) STO (100) and (b) STO (111) substrates, respectively. (c) XRD ω -scans performed about the PZT (101) plane and (d) XRD ω -scans performed about the PZT (002) plane for PLZT thin films grown on STO (100) substrates, respectively. (e) Room temperature Raman spectra for PLZT thin films grown on STO (100) substrates. Insets to (a) and (b) show the details of the STO and LSMO peaks at small 2θ ranges.

FIG. 2. Lattice parameters and tetragonality in $(\text{Pb}_{1-x}\text{La}_x)(\text{Zr}_{0.52}\text{Ti}_{0.48})\text{O}_3$ (PLZT) thin films with varying La concentrations of 0 at. %, 0.1 at. %, 0.5 at. % and 1.0 at. %; denoted as undoped PZT, 0.1 at. % PLZT, 0.5 at. % PLZT and 1.0 at. % PLZT, respectively. XRD symmetric θ - 2θ scans performed about the PZT (002) and PZT (111) planes for PLZT thin films grown on (a) STO (100) and (b) STO (111) substrates, respectively. (c) XRD asymmetric 2θ - ω scans performed about the PZT (111) plane for PLZT thin films grown on STO (100) substrates. (d) Lattice parameters (a and c) and tetragonality (c/a) in PLZT(001) and PLZT(111) thin films. (e) Reciprocal space map performed about STO (103) for 0.5 at. % PLZT thin film grown on LSMO/STO (100) substrate. The LSMO (103), STO (103) and PLZT (103) peaks are labelled. The position of the bulk is indicated with a red cross. Intensities from low to high: blue, green, yellow, red, brown.

FIG. 3.(a) Cross-sectional TEM image of the 0.5 at. % $(\text{Pb}_{1-x}\text{La}_x)(\text{Zr}_{0.52}\text{Ti}_{0.48})\text{O}_3$ (PLZT) thin film grown on LSMO bottom electrode on SrTiO_3 (STO) (100) substrate. HRTEM images of (b) PLZT-LSMO interface and (c) PLZT layer captured from the regions marked with red and blue boxes in (a) of the 0.5 at. % PLZT film. The images in (b) and (c) have been captured with the electron beam parallel to the [011] direction of the PLZT lattice. The crystal planes in both PLZT and LSMO have been marked with arrows. (d, e) SAED patterns captured near the PLZT-LSMO interface of the (d) 0.5 at. % PLZT film and (e) the undoped PZT film, respectively. The direction of the c-axis and the tetragonal symmetry of the PZT unit cell has been indicated by the white box and arrow. Comparing the white boxes in (c) and (d) a larger tetragonality of the PLZT unit cell can be observed as compared to undoped PZT unit cell. The arrows in (e) indicate the slightly mismatched lattice parameter of PZT and LSMO. (f) Typical AFM image of the PLZT (001) layer exhibiting the smooth particulate-free surface with low roughness ($R_{\text{rms}} \sim 4$ nm) and uniform grains of sizes $\sim 170 \pm 10$ nm captured from the 0.5 at. % PLZT (001) film.

FIG. 4.(a, b) Polarization versus electric field (P-E) curves for undoped PZT, 0.1 at. % PLZT ($\text{Pb}_{1-x}\text{La}_x\text{Zr}_{0.52}\text{Ti}_{0.48}\text{O}_3$), 0.5 at. % PLZT, and 1 at. % PLZT thin films grown along (001) and (111) orientations, respectively, measured at driving voltage of 9 V. Insets to (a) and (b) show the schematic diagrams of the capacitor geometries with LSMO as top and bottom electrodes.

FIG. 5. Correlation between lattice distortion and polarization in PLZT thin films. (a) Plots of squares of remanent polarization (P_r) and lattice distortion ($c/a - 1$) in the PLZT thin films grown along (001) and (111) orientations, denoted as PLZT (001) and PLZT(111), respectively. The linear fits of the data are also shown by red and blue lines.(b) Schematic illustration depicting the

enhancement in tetragonality in the undoped PZT unit cell as a result of substitutional doping of La^{3+} in the Pb^{2+} sites in the PLZT unit cell (shown by curved blue arrows) and the creation of defect dipoles between the substituted La^{3+} and $\text{V}_{\text{Pb}}^{2+}$ dipoles within the PLZT unit cell (shown by straight upright violet arrow). The direction of applied field is shown by red arrow.

Figure 1

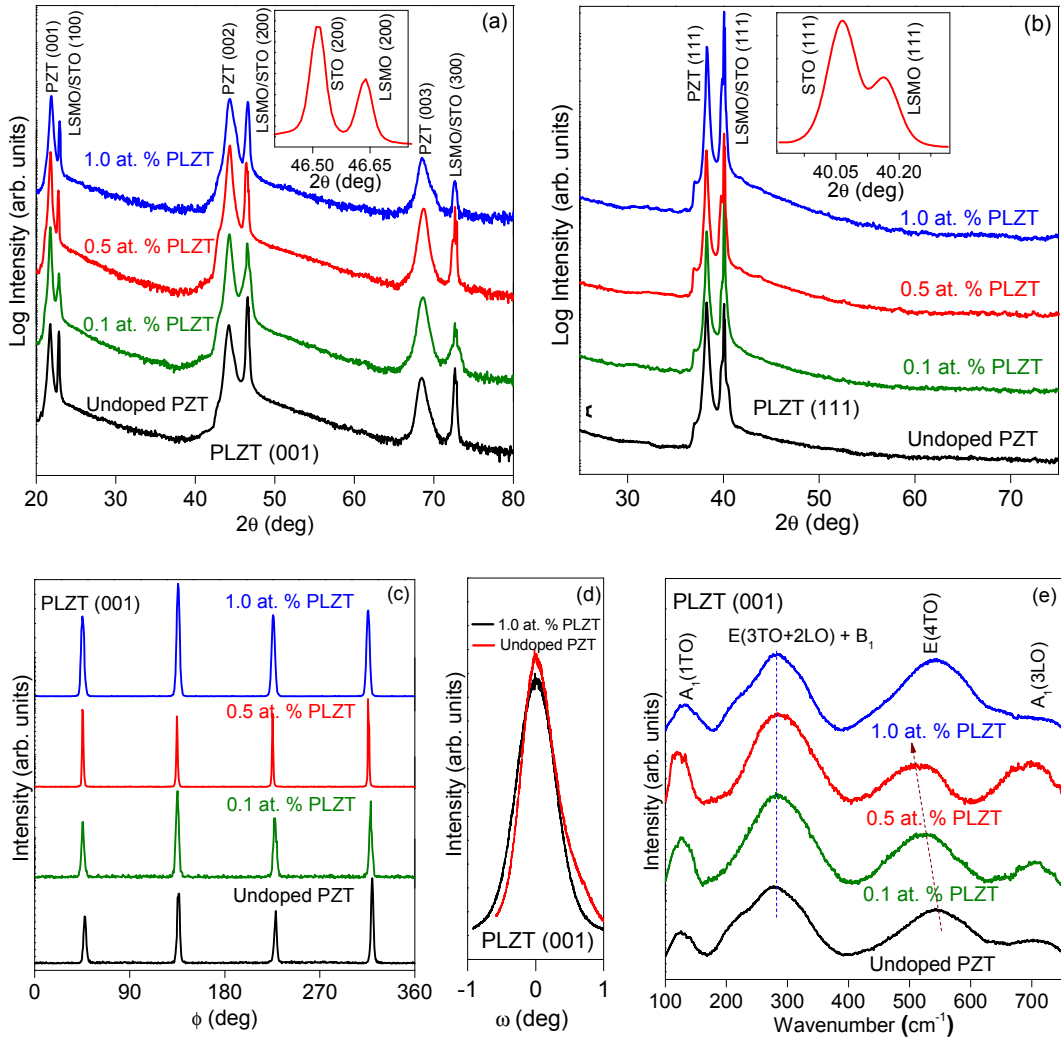


Figure 2

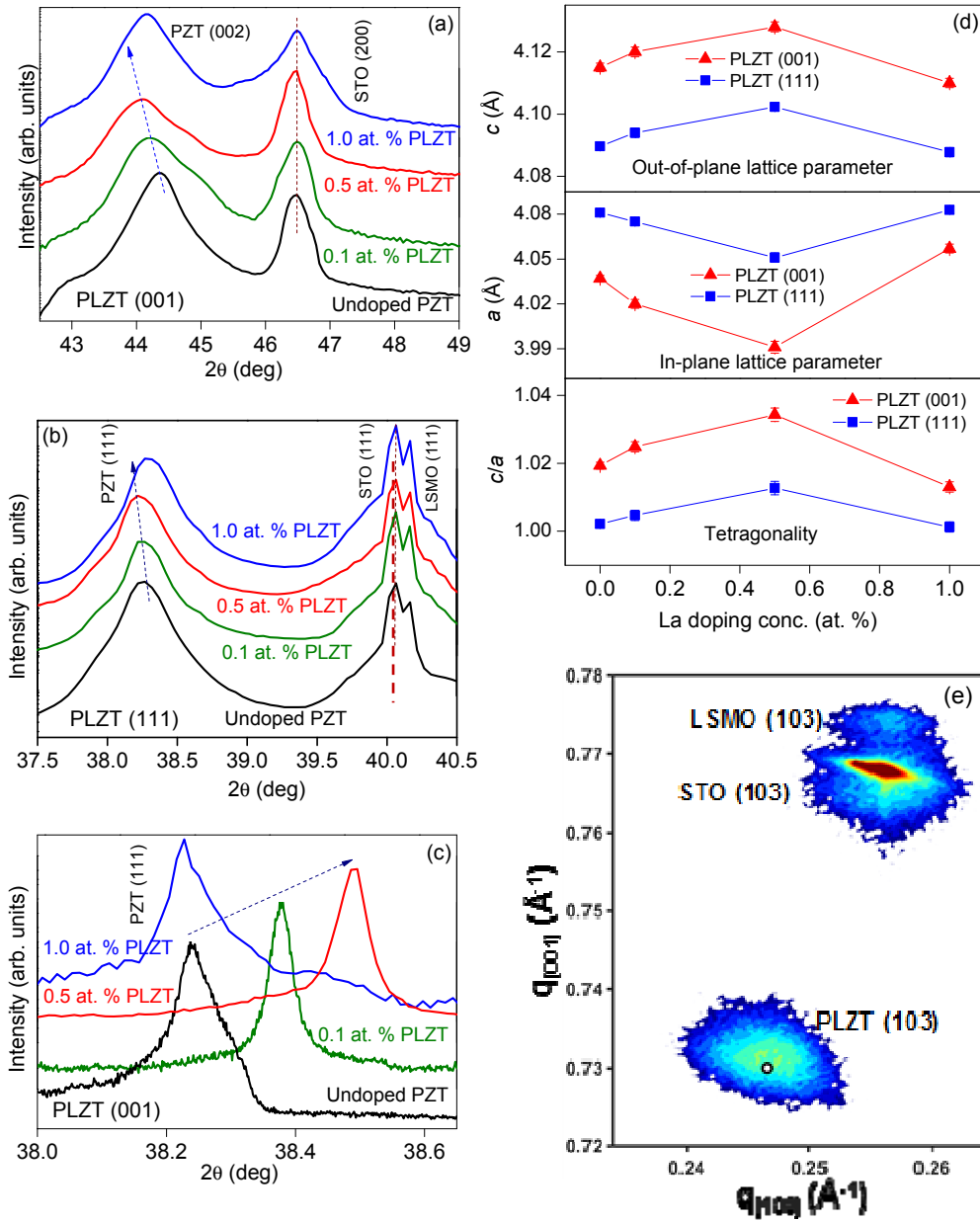


Figure 3

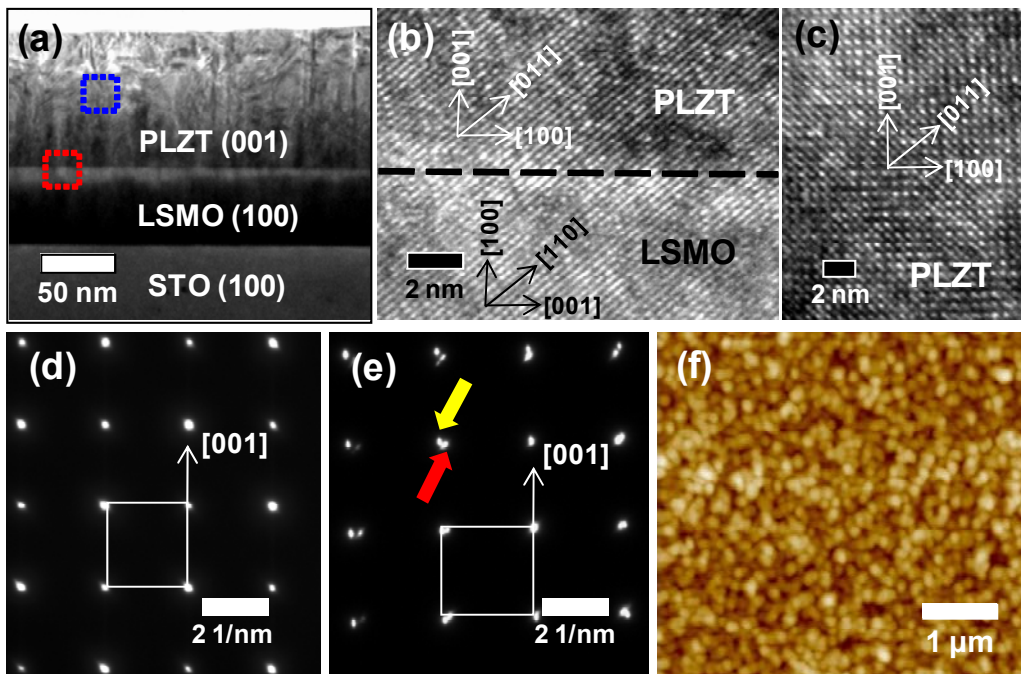


Figure 4

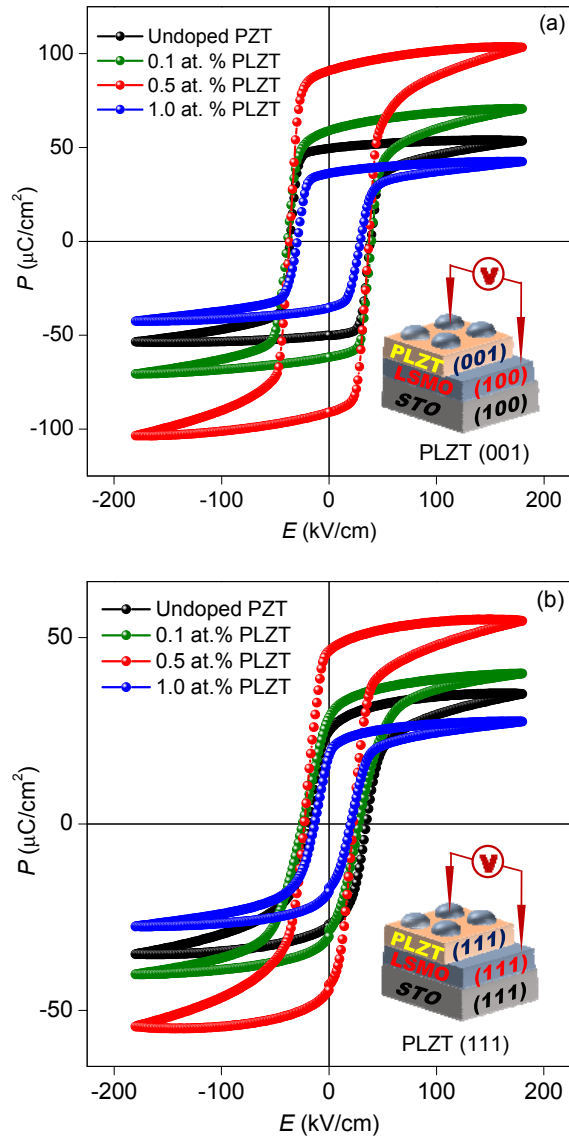


Figure 5

